Energy & Environmental Science

ROYAL SOCIETY OF CHEMISTRY

PAPER

View Article Online
View Journal | View Issue

Cite this: *Energy Environ. Sci.*, 2026, **19**, 1996

Reductive electron redistribution enables ultrafast charging in magnesium batteries

Wenbin Wang, Hongyu Zhang,* Miao Guo, Chaoqun Li, Xian Zhou, Guanglin Xia and Xuebin Yu *

Received 23rd October 2025,
Accepted 22nd January 2026

DOI: 10.1039/d5ee06320e

rsc.li/ees

Solvation sheath rearrangement is recognized as a key strategy for modifying electrolytes to enhance the kinetics of magnesium batteries. However, its fundamental mechanism diverges significantly from that in Li-ion batteries and remains inadequately understood. Herein, we elucidate the principle that solvation tuning essentially determines the distribution of reductive electrons, whose accumulation on ether molecules directly leads to challenging reorganization and severe solvent decomposition. To address this, a series of organic monoamine salts are designed as additives to capture and stabilize the reductive electrons in the solvation sheath, and screening guidelines are proposed to promote the kinetics and reversibility of Mg plating/stripping. Accordingly, we demonstrate an Mg pouch cell with ultrahigh power density (50C, 13 mA cm^{-2}, 16.02 kW kg^{-1} based on the cathode), surpassing the power densities reported in all previous studies. This work offers new insights into solvation tuning strategies that are crucial in designing high-power-density Mg batteries.

Broader context

Rechargeable magnesium batteries are regarded as potential substitutes to Li-ion batteries due to the abundance, safety, and high volumetric capacity of Mg. However, their electrochemical performance remains limited by the sluggish Mg^{2+} de-solvation process at the electrode/electrolyte interface. Although significant progress has been made in electrolyte additive strategies, there remains substantial room for deeper understanding of the underlying mechanisms. In this work, we find out that the ether molecules in the solvation sheath struggle to stablize obtained reductive electrons, which fundamentally leads to the challenging solvation sheath reorganization and high energy barrier of Mg^{2+} de-solvation process. To overcome this challenge, we introduce monoamines into the electrolyte, which are computationally and experimentally demonstrated to receive reductive electrons and effectively lower the energy barrier for the Mg^{2+} de-solvation process. Besides, the guidelines for additive screening are developed to enhance the performance of electrolytes. Based on them, we greatly improved Mg electrolyte performance. Mg pouch cells assembled with these electrolytes can tolerate huge current and have an unprecedent power density two orders higher than all previous reports. This work not only explains the principles of Mg^{2+} solvation sheath rearrangement, providing invaluable insights for the design of Mg electrolytes, but also vastly improves the power density of pouch cells, thereby profoundly advancing the practical application of Mg metal batteries.

Introduction

The explosive expansion in electric vehicles has posed unprecedented demands on the development of next-generation energy storage batteries.[1–3] With higher theoretical capacity, divalent metal batteries garner extensive research interest. Among them, magnesium metal batteries (MMBs) stand out owing to their abundance in the Earth's crust, dendrite-free nature, high volumetric capacity (3832 mA h cm^{-3}), and low reduction potential (−2.38 V *vs.* standard hydrogen electrode), and they have been regarded as one of the most promising alternatives to Li-ion batteries (LIBs).[4,5] However, the electrolytes used in MMBs still suffer from significant limitations. Despite considerable progress, it remains challenging for the relatively widely used aluminum chloride complex and boron-based magnesium electrolytes to achieve the features of low cost, simple synthesis, and high anodic stability simultaneously.[6–11] Therefore, simple salt electrolytes draw intensive attention due to their high anodic stability, low cost and facile synthesis.

Unfortunately, the intrinsic sluggish kinetics of Mg^{2+} in the de-solvation process, as well as the accompanying surface passivation induced by electrolyte decomposition, could result in large polarization and severely affect the electrochemical performance of MMBs upon using conventional Mg electrolytes containing simple salts (*e.g.* magnesium bis-(trifluoromethanesulfonimide) [$Mg(TFSI)_2$]), which highly restricts their further application.[12–14] Similar to LIBs, the introduction of suitable additives has been explored to rearrange the solvation sheath, aiming to facilitate the challenging de-solvation process.[15–17]

Department of Materials Science, Fudan University, 220 Handan Road, Shanghai, China. E-mail: zhang_hongyu@fudan.edu.cn, yuxuebin@fudan.edu.cn

Although noticeable progress has been made, research on how Mg^{2+} solvation sheath rearrangement fundamentally affects the de-solvation process remains insufficient, which should be way different from that in LIBs.[18–20] This uncertainty poses challenges for the design of high-kinetic Mg electrolytes. Recently, some organic monoamines have been identified as excellent additives, which could significantly reduce the overpotential of Mg plating/stripping.[21–24] However, the low polarization achieved in these works was frequently accomplished at the expense of abnormally low coulombic efficiency (CE), leading to the degradation of cycling stability. Furthermore, despite the modification, the kinetics of the de-solvation process are still insufficient to satisfy the assembly of pouch cells with high power density. More importantly, previous studies often focus on the interlayer formed on the Mg anode, while how these monoamines function in the solvation sheath has not been thoroughly investigated and convincingly concluded. In general, unraveling the basic principles of solvation sheath rearrangement and reporting the screening guidelines for appropriate additives to precisely tune the solvation sheath continue to be a perplexing but pivotal task for Mg electrolytes.

In this study, we demonstrate that the solvation sheath rearrangement essentially alters the distribution of reductive electrons, which are challenging for the ether molecules to stabilize. It directly creates high energy barrier and sluggish kinetics due to the large deformation and severe decomposition of these solvent molecules. Therefore, a series of organic monoamine salts are selected as the solvation sheath rearrangement additives to capture the reductive electrons from ether molecules and facilitate the reorganization process, thereby reducing the energy barriers and improving the kinetics. Moreover, the screening guideline of these monoamine additives is proposed to develop MMBs with excellent kinetics and reversibility. The electrolyte modified with tetramethyl amine hydrochloride exhibits low overpotential (<140 mV) and high CE ($>99\%$), allowing for an at-most 20-mAh pouch cell with an ultrahigh power density of 16.02 kW kg^{-1} (50C, 13 mA cm^{-2}), surpassing that of all the other reported Mg pouch cells. Our work not only provides guidance for the design of fast-kinetic Mg electrolytes but also strongly promotes the potential commercial application of MMBs in the future.

Results

De-solvation process alteration

The Mg^{2+} solvation sheath in simple salt electrolytes is nearly completely occupied by ether molecules such as DME.[25,26] Therefore, $[Mg(DME)_3]^{2+}$ is regarded as the main active species in the commercially available 0.5-M $Mg(TFSI)_2$-DME solution, which is frequently used in the production of Mg batteries and chosen as the blank electrolyte in this work. According to previous researches, the de-solvation process of solvated species (*e.g.* $[Mg(DME)_3]^{2+}$) could be divided into two stages:[21,27] first, the reductive electrons transfer, while the solvation sheath reorganizes its structure (*e.g.* $[Mg(DME)_3]^{+}$). Second, the restructured solvation sheath decoordinates and releases a ligand to achieve a more stable state (*e.g.* $[Mg(DME)_2]^{+}$). Notably, although the whole de-solvation process takes place at the surface of the Mg anode, the deposition of Mg atoms is not a rate-determining process and does not substantially vary in different electrolytes; hence, it is not discussed in detail.[21,28] To gain deeper comprehension of the de-solvation process, the structures of differently charged solvation sheaths are calculated based on the density functional theory (DFT) (Fig. 1A). It reveals that after obtaining reductive electrons, the DME molecules in the reorganized solvation sheath tend to suffer from severe deformation and even chemical bond breaking. The accompanying decomposition eventually leads to the generation of passivation layers (*e.g.* MgO, $Mg(OH)_2$) on the surface of the Mg anode, which would block Mg^{2+} transportation. This could be one of the direct reasons for the huge overpotential during Mg plating/stripping, as shown in many reported works.[29]

Organic amine additives were reported to be effective in promoting the de-solvation process of Mg^{2+}, despite being plagued by unsatisfactory CE and rate performance.[21–24] To fundamentally study and uncover the mystery of monoamine additives in improving the electrochemical performance of MMB, some methylamine salts were added to the blank electrolyte. The simplest organic monoamine methylamine, along with other monoamines with more substituted methyl, was selected as additive to the blank electrolyte, while the formed solution was regarded as the experimental group. NC1, NC2, NC3, and NC4 represent the blank electrolyte with 1.0 M methyl, dimethyl, trimethyl, and tetramethyl amine hydrochloride added groups, respectively.

Previous research and high-resolution mass spectrum (HR-MS) results have proved the coexistence of monoamine molecules and cations in these electrolytes (Fig. S1).[23,24,30] The electrostatic potential of these monoamines was calculated to be more negative than those of the solvent molecules, which demonstrates their stronger interaction with Mg^{2+} and their potential to enter the solvation sheath (Fig. S2). Also, according to previous research, Mg^{2+} tends to form $MgCl^{+}$ as a complex cation in such Cl-containing electrolytes (Fig. S3).[6,31,32] Besides, based on the six-fold coordination of Mg^{2+} and binding energy calculations, $[MgCl(NCx)(DME)_2]^{+}$ could be regarded as the most potential solvation sheath structure in the electrolyte, being used for further calculations (Fig. S4 and Tables S1, S2). The EIS-MS results of the NC1 electrolyte could also confirm such structures (Fig. S1).

On account of this, structural and energy calculations were performed for all the monoamine-added groups. Results showed that the reorganization process of the experimental groups was evidently different from that of the blank group. In monoamine-involved electrolytes, the DME molecules stay much more stable after receiving a reductive electron, and unexpected chemical bond breaking is also markedly inhibited (Fig. 1B and Fig. S5). Besides, *ab initio* molecular dynamic (AIMD) simulations were conducted to dynamically portray the reorganization process of the solvation sheath. It turned out that the DME molecules in $[Mg(DME)_3]^{+}$, the reduced solvation sheath in the blank group, were greatly distorted only

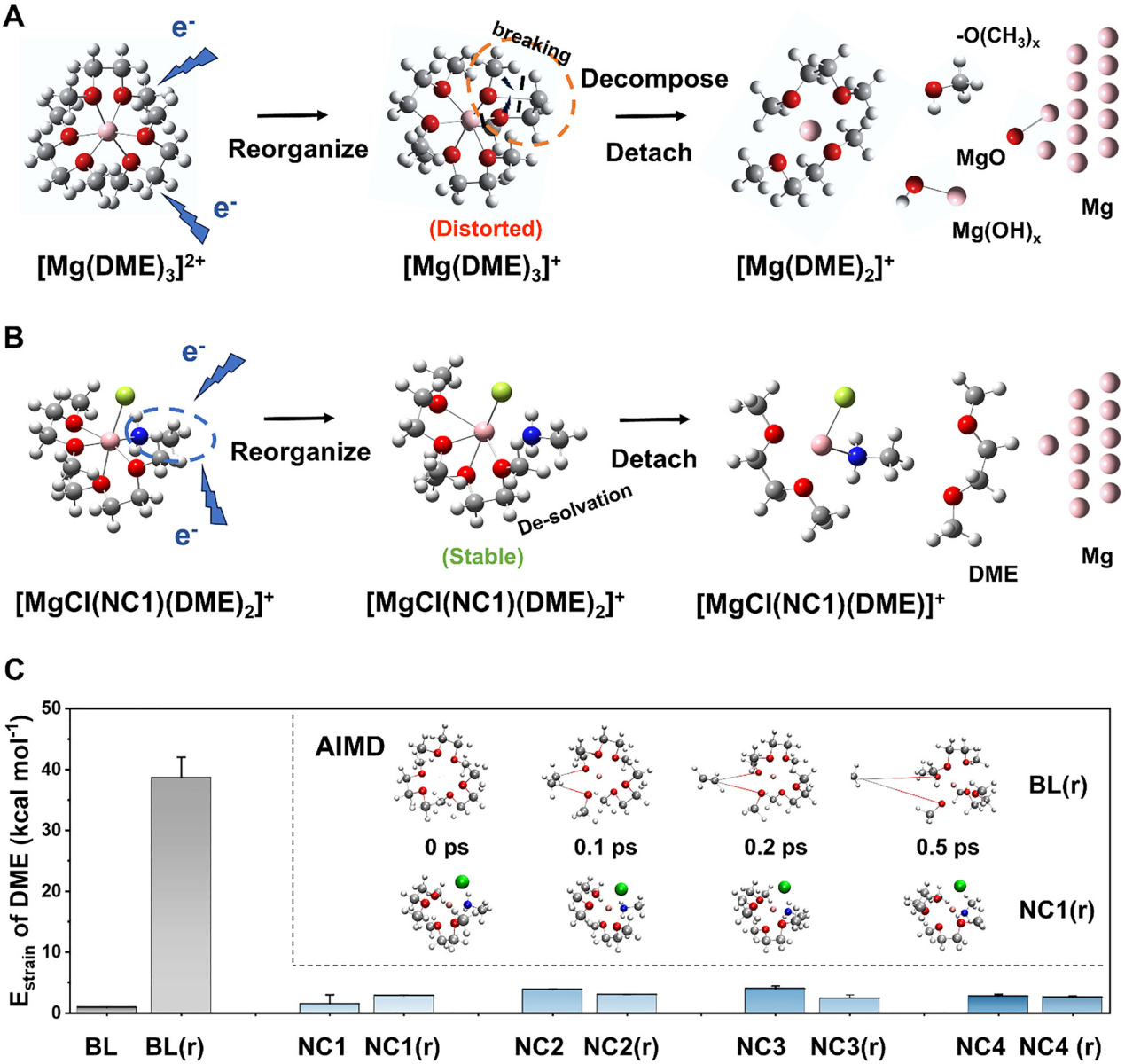

Fig. 1 Illustration of the de-solvation process. Calculated de-solvation process of $[Mg(DME)_3]^{2+}$ (A) and $[MgCl(NC1)(DME)_2]^{+}$ (B). (C) Average strain energy of DME molecules in the solvation sheath after obtaining a reductive electron. (Inset of Fig. 1C: AIMD simulations of $[Mg(DME)_3]^{+}$ and $[Mg(NC1)(DME)_2]^{+}$). The letter "r" refers to the solvation sheath after obtaining one reductive electron. The red, green, grey, blue and white balls refer to the O, Cl, C, N and H atoms, respectively.

after 0.1 ps (Fig. 1C), whereas the DME molecules in the monoamine-involved solvation sheath remained relatively stable during the whole simulation process, despite their tendency to desolvate (Fig. S6). This result further confirmed that monoamine in the solvation sheath could suppress the deformation of DME molecules, thereby reducing extra reorganization energy. To quantitatively evaluate the degree of molecule deformation, the average strain energy calculations of DME molecules in the solvation sheath (E_{strain}) before and after receiving one electron were calculated (Fig. 1C and Table S3). The E_{strain} after the reduction in the blank electrolyte was much higher than those in the experimental electrolytes, while no evident difference was observed among all unreduced groups. These results explain that the DME molecules in blank electrolyte would undergo serious deformation and decomposition during the de-solvation process, while those with monoamines involved would avoid mostly. This could be the direct reason for the improved performance in monoamine-involved electrolytes.

Basic mechanistic analysis

The energy barriers for reorganization and decoordination, denoted as $\Delta G_1^{\neq}$ and $\Delta G_2^{\neq}$, respectively, were calculated to analyze the de-solvation process quantitatively according to the Marcus theory (Fig. S7 and S8).[33,34] $\Delta G_1^{\neq}$ revealed the difficulty of solvation structure reorganization after obtaining a reductive electron. Besides, $\Delta G_2^{\neq}$ quantified the obstacle for

rearranged solvation structures to dissociate a coordination site of DME (Fig. S9 and S10). According to the calculations, the $\Delta G_1^{\neq}$ and $\Delta G_2^{\neq}$ of all the experimental groups dropped considerably compared with the blank group.

With both the reorganization and decoordination processes considered, the energy barrier ranked as NC1 < NC2 < NC4 < NC3 ≪ blank group (Fig. 2A, B, and Table S4). Overall, the blank electrolyte was faced with much more obstacles during the de-solvation process compared with the experimental groups added with monoamine salts. Combining the results in Fig. 1, these huge energy barrier differences are thought to be triggered by the deformation of DME molecules.

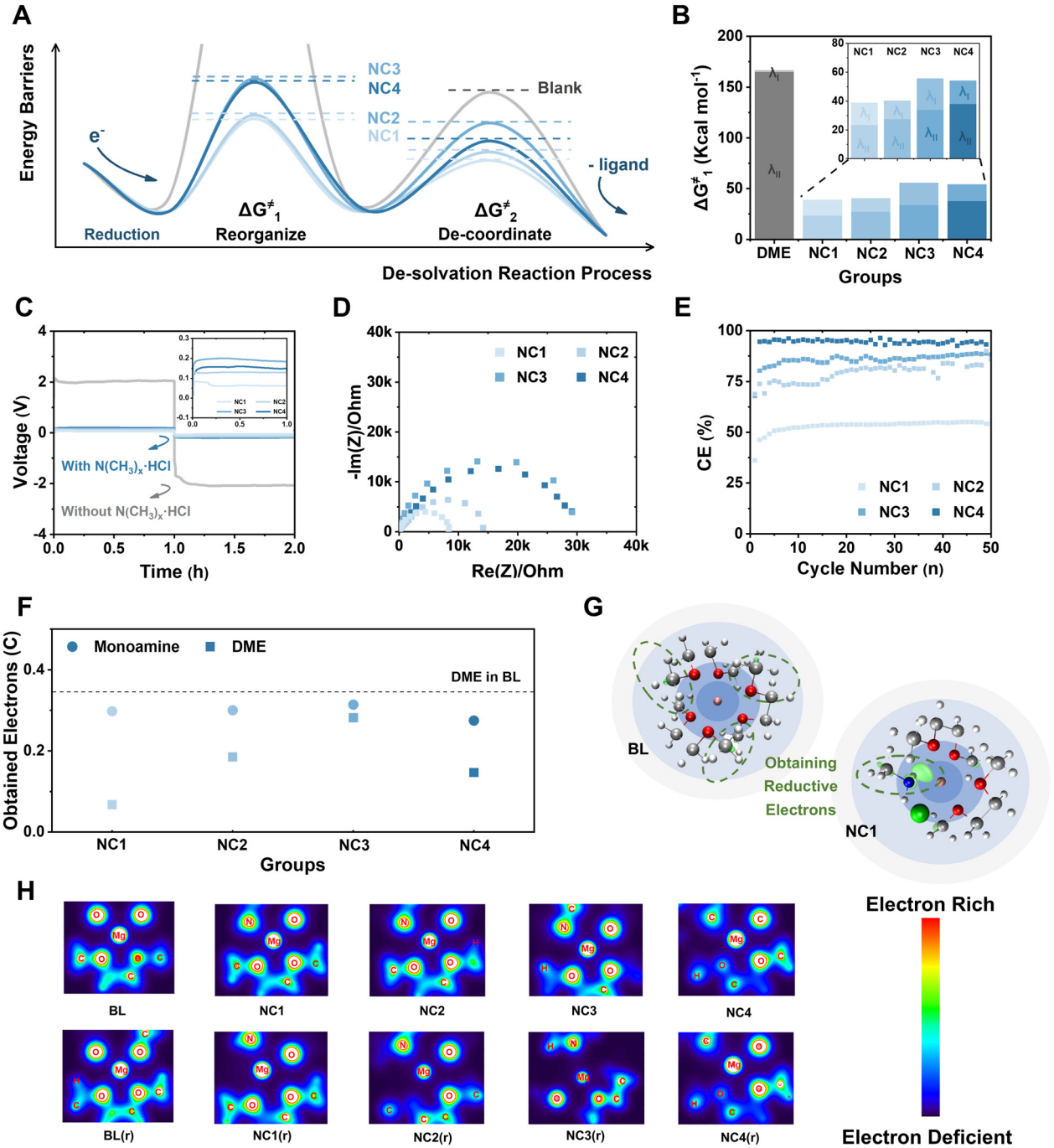

Fig. 2 Mechanism exploration by solvation tuning. (A) Calculated energy barriers of the de-solvation and reorganization processes. (B) Detailed energy barrier calculation in the experimental and blank groups. (C) Voltage curves of the Mg||Mg symmetry cells with different electrolytes at 0.1 mA cm^{-2} and 0.1 mAh cm^{-2}. (D) PEIS spectra of the Mg||Mg symmetry cells with different electrolytes. (E) Coulombic efficiency of the Mg||SS half cells with different electrolytes. (F) Calculated electrons of the DME molecule and monoamines in the reduction process. (G) Electron density difference plots between the solvation sheath before/after obtaining a reductive electron in NC1 and the blank group. Green parts are the places where the reductive electron distribution varies. (H) Colored contour map of the electron density difference of solvation sheath in the experimental and blank groups.

In theory, the significantly reduced energy barrier would lead to facilitated kinetics, further reducing the overpotential and improving the rate performance. To prove these assumptions, electrochemical performance tests were carried out on the blank and experimental groups. A marked decrease in overpotential in the Mg plating/stripping process was observed when the organic monoamine salts were introduced (Fig. 2C and Fig. S11). NC1 shows the unprecedentedly lowest overpotential for the Mg electrolyte (<60 mV), while NC3 has the highest (~200 mV). Notably, the increase in overpotential was not totally monotonic, which aligns with the energy barrier calculations in Fig. 2A (NC1 < NC2 < NC4 < NC3). Besides, potentiostatic electrochemical impedance spectroscopy (PEIS) measurements showed that the cation transfer kinetics in symmetric cells also agrees with the overpotential results (Fig. 2D). Furthermore, electrolytes added with monoamine were found to possess higher ionic conductivity, which demonstrate that the introduction of organic monoamine salts enhances the Mg^{2+} transport in the electrolyte. The ohmic polarization of both experimental and blank groups was calculated to be negligible (Fig. S12 and Table S5). On the other hand, CE in various electrolytes was tested in Mg||stainless-steel (SS) half cells, which varied considerably in different groups (Fig. 2E and Fig. S13, S14): NC1, the group with the lowest polarization, exhibited the lowest CE (~55%). Besides, the CE of the experimental groups rose linearly as the number of methyl substitutions increased, while the NC4 electrolyte exhibited the highest CE, nearly 100% in the CV tests. CE tests using the cyclic voltammetry method also draw similar conclusions, showing the accuracy of our measurements (Fig. S15 and S16).

On account of these calculations and experiments, the energy barrier observed for the de-solvation process was consistent with the electrochemical test results. It is the involvement of monoamines that rearranges the solvation sheath, thereby relieving the solvent molecule deformation and reducing the energy barrier. However, the fundamental reasons for the huge difference still require additional investigation. Based on our analysis on the de-solvation process, the solvation sheath structure becomes unstable after receiving reductive electrons. Therefore, the obtained charges of the different solvation sheath fragments in the reduction process were calculated (Fig. 2F). The results indicated that, relative to those in the experimental groups, the DME molecules in the blank group obtained more reductive electrons during reduction. Also, the monoamines tended to obtain more reductive electrons than the DME molecules. In particular, the DME molecule in the NC1 electrolyte gained relatively fewer electrons after the reduction. It can be speculated that the monoamines in the solvation sheath received reductive electrons during the reorganization process.

To further elucidate this phenomenon, the electron density difference plots between the reduced/unreduced states were compared. In the blank group, the reductive electrons acquired by the solvation sheath were dispersedly distributed on the DME molecules, especially on the C atoms, and these molecules were thus deformed. Contrarily, in the NC1 group, the reductive electrons acquired during the reduction process mainly gathered on the N atoms (Fig. 2G). The outcomes in other experimental groups resembled that in NC1, which demonstrated that monoamines were much more attractive to electrons than ether, rendering DME molecules relatively electron-deficient and less distorted (Fig. S17). The colored contour maps of the electron density show the electron distribution more clearly. This implies that reductive electrons are more likely to accumulate on the N and contiguous C atoms of monoamines, with no evident chemical bond deformation. Comparatively, both the electron distribution and molecular structure of DME in the blank group were altered significantly after receiving electrons, revealing that it is challenging for DME molecules to stabilize reductive electrons (Fig. 2H). These differences in electron distribution are easy to understand: the electron orbitals of O atom are already filled with lone pairs of electrons, thus facing difficulty stabilizing additional ones obtained in the reduction process. To accommodate the reductive electrons, the structure needs to be drastically altered and even disrupted, which gives rise to high reorganization energy barriers. In comparison, the strong interaction and unoccupied orbits of the N atom in monoamines enable it to acquire the reductive electrons preferentially and stabilize them without too much molecule deformation. It dramatically reduces the energy barrier and promotes the kinetics of the monoamine-involved electrolyte.

Besides, the use of monoamine hydrochloride salts, rather than monoamines, is impractical because organic amines are always gaseous at room temperature, which makes it hard to control the concentration and complete elimination of trace water. Therefore, the role of Cl^- in the electrolyte should be discussed in detail to address these concerns. According to a previous study, the Cl^- in these electrolytes tends to be beneficial to charge transfer and passivation inhibition.[32,35,36] However, the improvement is likely to be insignificant: although both the overpotential and impedance of the blank electrolyte decrease after the addition of $MgCl_2$, the effect is not that prominent (Fig. S18). On the other hand, if only 1.0 M propylamine, rathan than propylamine hydrochloride salts, is added into the blank electrolyte, the overpotential would be only about 75 mV, similar to that of experimental groups (Fig. S19). Additionally, the solvation sheath structure, de-solvation energy barrier and electron distribution situation in the solvation sheath when Cl^- is not taken into consideration were calculated, and the conclusions are identical (Fig. S20–S25). In a word, although Cl^- is beneficial to the improvement of the stability and electrochemical performance of the electrolyte to some extent, monoamines play a much more decisive role, and it does not affect our discussion.

Moreover, to confirm the relationship between energy barrier and reductive electron distribution, monoamines with specific electron-stabilizing conjugate structures were also chosen as solvation sheath rearrangement additives, including aniline hydrochloride (PhN) and allylamine hydrochloride (AlN), which are supposed to display improved de-solvation kinetics. Both groups display a hugely declined overpotential in

Mg||Mg symmetry cells, although the CE is not very satisfactory (Fig. S26 and S27). The DFT calculations on the energy barrier of these two groups also agreed well with the experimental results (Table S6).

In conclusion, the involvement of monoamine into the solvation sheath could help redistribute and stabilize the reductive electrons that would otherwise lead to the decomposition of ether molecules. It could fundamentally avoid the huge deformation and decomposition of ether molecules at a reduced state, hence promoting the reorganization process and reducing passivation layer formation on the Mg metal anode. We conducted scanning electron microscopy (SEM) on the cycled Mg anodes. The results show that those cycled in the blank electrolyte suffer from severe non-uniform deposition, while the Mg deposition in the NC4 electrolyte is much more even. Moreover, scanning electron microscopy–energy-dispersive spectroscopy (SEM-EDS) showed that there were less S, F, and O on the surface of the Mg anode cycled in experimental electrolytes, implying the suppressed decomposition of $TFSI^-$ and DME. (Fig. S28 and S29).

Side-reaction inhibition

Generally, the low coulombic efficiency in $Mg(TFSI)_2$-based electrolytes is attributed to the decomposition of solvents and $TFSI^-$, as demonstrated in Fig. 1a. It results in the generation of side products, such as MgO and $Mg(OH)_2$, and organic products, passivating the anode surface and further hindering Mg^{2+} transportation[24,37]. Hence, in the absence of other side reactions, the overpotential and CE of Mg^{2+} stripping/plating should always be inversely correlated in theory. However, in this study, the observed trend does not follow this rule: as the alkyl substitution of the amine salt increases, the CE also increases, and the SEM results indicate that side reactions are further suppressed (Fig. S30). Meanwhile, the overpotential generally becomes higher. Specifically, the overpotential of NC1 is unprecedentedly less than 60 mV, while its coulombic efficiency is the lowest among all the experimental groups ($<60\%$), which contradicts with previous experience. It should be noted that the Raman spectra of $TFSI^-$ and DME revealed an evidently weakened interaction with Mg^{2+} in the experimental groups, particularly in the less-substituted groups (*e.g.* NC1 and NC2) (Fig. S31 and S32). Besides, the reductive electrons on solvent molecules were projected to be lower after the monoamine addition, which was supposed to be favorable for suppressing the decomposition (Fig. 2F–H). These facts imply that the fundamental reason for the decrease in CE may not be the decomposition of $TFSI^-$ or the solvent, but rather the organic monoamines. Monoamines may not only share and redistribute reductive electrons during the de-solvation process but also bear the risk of being reduced themselves, generating side products. To identify the ideal design of the monoamine additive, it is necessary to investigate the existence form of the side products and their generating mechanism.

The existence form of side products was identified *via* X-ray photoelectron spectroscopy (XPS). Except for $TFSI^-$ residues, ammonium cations generated from the decomposition were the predominant N species on the surface of the cycled Mg anode (Fig. 3A and Table S7). These cations were generated by the decomposition of monoamines during the electrochemical process, because there would be no such peaks if the Mg anode was only soaked in the electrolyte (Fig. S33). Notably, the signal intensity of ammonium cations in the experimental groups decreased from NC1 to NC4, indicating a progressively weakened side reaction.[38,39] Also, the potential decomposition products of $TFSI^-$, including F^-, S^{2-} and O^{2-}, were reduced relatively to the blank electrolyte according to the XPS spectra (Fig. S34).[40,41] The results of the time-of-flight secondary ion mass spectrometry (TOF-SIMS) of NC1 and NC4 agreed well with the XPS results. After the normalization process based on Cl^- signal, the signal of NH_2^- was much stronger on the surface of the Mg anode cycled in NC1 than that in NC4 (Fig. 3B and Fig. S35). Moreover, we soaked the Mg anode, which had undergone cycling in different electrolytes, in 50 mL of H_2O to form a solution, and the ammonia concentration was assessed *via* ion chromatography (IC). Mg anode in different experimental groups in 50 mL of H_2O. The results further confirmed that the concentration of NH_4^+ in the solution decreased from NC1 to NC4 (Fig. 3C and Fig. S36). Additionally, a colorimetric kit for measuring ammonia concentration was utilized to quantify the concentration produced on the Mg anode surface more intuitively. It directly shows the ammonia concentration declines from NC1 to NC4, and in all groups it increases as cycles (Fig. 3D and Fig. S37). In conclusion, ammonia was the main side product in the electrolytes containing monoamines, and the side reaction could be generally suppressed with increased substituted $-CH_3$ groups.

To explain this phenomenon, classic molecule dynamic (c-MD) simulations were performed to evaluate the interaction between Mg^{2+} and monoamines (Fig. 3E and Fig. S38, S39). It turned out that NC1 and NC2 could strongly solvate with Mg^{2+} (<0.2 nm), whereas NC3 and NC4 maintain a medium interaction. In comparison, the DME molecules and $TFSI^-$ were less prevalent in the solvation sheath for all experimental groups (Fig. S40). It appeared that the interaction distance was related to the side reactions. NC1 and NC2, which were closely involved in the solvation sheath, suffered from severe side reactions, whereas monoamines with larger contact distances tended to be eased.

To examine the hypothesis, propylamine hydrochloride (3CN) and methoxyamine hydrochloride (CON) were selected as additives, whose interaction distance to Mg^{2+} was manipulated by altering the steric hindrance and electronegativity, respectively (Fig. S40, S41 and Table S6). Both these two groups have longer interaction distance to Mg^{2+} relative to NC1, and they display a relatively higher CE despite a higher overpotential, which is also consistent with the calculation results. These findings support the idea that a longer interaction distance between Mg^{2+} and monoamines could reduce the side reactions.

In general, the solvation reorganization and side reaction are largely determined by the interaction distance and interaction strength between Mg^{2+} and monoamines: a closer interaction distance leads to the easy formation of Mg–N bond and decomposition of monoamines, which always results in

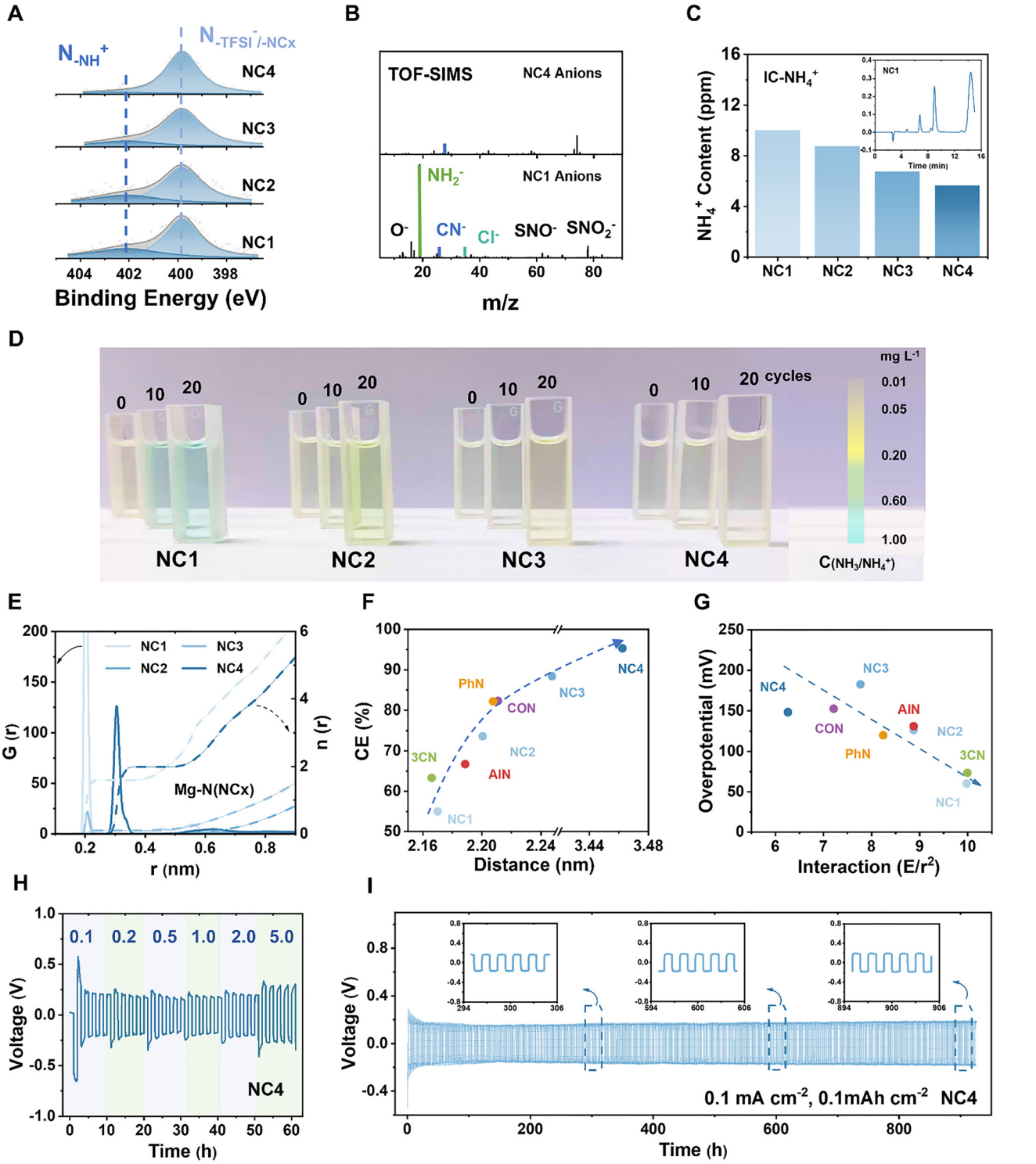

Fig. 3 Side reaction inhibition and additive screening. (A) N 1s XPS spectra of the Mg anode cycled in the experimental groups. (B) ToF-SIMS spectra of the cycled Mg anode in the NC1 and NC4 groups. Ammonia concentrations of the solution soaking the Mg anode cycled in the experimental groups tested by IC spectra (C) and ammonia concentration kit (D). (Inset of Fig. 3C: IC spectra of the solution soaking the Mg anode cycled in NC1 group) (E) radical distribution function of the N atom in monoamines calculated by c-MD. Correlation analysis between CE and interaction distance (F) and overpotential and interaction strength (G) among all the groups. (H) Rate performance of the Mg||Mg symmetry cells with the NC4 electrolyte. (I) Long-term cycling of the Mg||Mg symmetry cells with the NC4 electrolyte at 0.1 mA cm^{-2} and 0.1 mAh cm^{-2}.

decreased CE. At the same time, a closer interaction distance often means stronger interaction strength, and the solvation sheath rearrangement and reductive electron redistribution would be more effective, thereby reducing polarization.[24,42] Therefore, a balance needs to be found to accomplish satisfactory overpotential and CE simultaneously, when amine-based additives have relatively longer interaction distance and high interaction strength. As a result, the screening guideline for monoamine additives are established, which could be identified based on these two factors. The calculated distance between Mg^{2+} and N atom is regarded as the interaction distance (r), while the interaction strength between Mg^{2+} and monoamine is essentially coulombic, which could be evaluated by the electrostatic potential divided by distance square (E/r^2). Although different functional groups of the monoamines could also have a slight influence on the reductive electron distribution, these two are the crucial factors, and all the monoamines in this work conform to the criteria (Fig. 3F, G and Fig. S43, Table S6). Also, it is noted that these guidelines remain applicable even without considering the participation of Cl^- (Fig. S44).

Combining all the calculations and experiments, NC4 stands out as the best monoamine additive in the work, capable of balancing solvation sheath rearrangement and side reaction inhibition. In Mg||Mg symmetry cell tests, the NC4 electrolyte exhibited excellent rate capability, which could endure high current density and areal capacity of up to 5 mA cm^{-2} and 5 mAh cm^{-2}, respectively, with no evident overpotential increase (Fig. 3H and Fig. S45). These Mg||Mg symmetry cells can also cycle at high capacity of several mAh cm^{-2} stably in the long term (Fig. S46). They also have superior adaptation to low temperature, allowing them to function even at a temperature of as low as −30 °C, the polarization of which maintains less than 300 mV (Fig. S47). Outstanding endurance to both high current and low temperature proves the greatly facilitated kinetics of the NC4 electrolyte. Moreover, in the long-term cycling performance test at 0.1 mA cm^{-2} and 0.1 mAh cm^{-2}, it remains stable for over 1000 h with an overpotential of less than 200 mV, showing its remarkable cycling stability (Fig. 3I). Besides, the NC4 electrolyte displays great oxidation stability on different current collectors and scanning rates. When SS and Ti serve as the current collectors, the anodic stability would be higher than 2.5 V and 3.9 V, respectively (Fig. S48 and S49). The promoted kinetics and prolonged voltage platform endow the electrolyte with wider cathode applicability.

Full-cell performance

To demonstrate the potential practical applications of the NC4 electrolyte, normal intercalation-type cathodes, Mo_6S_8 and $Cu_{2-x}Se$, for instance, were firstly tested at a high current density in the coin cell. After the conditioning process, the $Cu_{2-x}Se$ cathode not only displayed outstanding rate performance but also kept a specific capacity of more than 180.5 mAh g^{-1} at 5C after 400 cycles, showing excellent long-term cycling stability (Fig. 4A, B and Fig. S50–S53). By comparison, the large polarization and poor cycling stability in the blank electrolyte further explain the effects of monoamine additives (Fig. S54). Furthermore, the commonly used Mo_6S_8 cathode displayed exceptional rate capability and cycling stability with the NC4 electrolyte (100 mAh g^{-1}, 5C), surpassing those in previous research (Fig. S55–S58).

To further validate the feasibility of the modified electrolyte under practical conditions, the performance of the NC4 electrolyte was examined in the pouch cell with polyaniline cathode (PANI). Both the discharging curves and CV peaks showed a high voltage platform at around 2.0 V (Fig. 4C and Fig. S59). Taking advantage of the much lower overpotential in the NC4-containing electrolyte than in the blank electrolyte, the full cell shows an evident difference in voltage platform and specific capacity in the NC4 and blank electrolytes. After the electrolyte conditioning and cathode refinement in the activating process, the PANI cathode in NC4 achieved a specific capacity of 270 mAh g^{-1} with a low polarization of about 0.5 V, which was much superior to that in the blank group (Fig. 4C).

Moreover, a prototype Mg pouch cell with unparalleled 20 mAh at most could be achieved for over 175 cycles, indicating the potential of the NC4 electrolyte in high-capacity pouch cells (Fig. 4D and Fig. S60). The voltage platform of the pouch cells is identical regardless of what current they are cycling at, showing its brilliant stability. Despite the fact that CE would be slightly over 100% after multiple cycles, which is due to the unavoidable oxidation at a high voltage, the side reactions are overall controllable (Fig. S61–S63). More crucially, the much-promoted kinetics of the NC4 electrolyte endows the pouch cell with an outstanding rate performance of up to 50C (13 mA cm^{-2}), while the current obtained from the previous Mg pouch cells is always less than 0.5C (Fig. 4E). When cycling at 50C, the PANI cathode in the pouch cell still delivers a discharging capacity of 197.7 mAh g^{-1} and maintains capacity retention of 85.4% after 400 cycles (Fig. 4F and Fig. S63). The power density of the pouch cell reached 16.02 kW kg^{-1} based on the cathode (6.65 kW kg^{-1} based on the cathode and anode), which was significantly higher than all the previous Mg pouch cells according to our estimations, showing broad application prospects (Fig. 4G and Fig. S64, Tables S8–S11).[11,43–54] Also, even if tested at high loading and smaller currents, the PANI cathode still show similar voltage platform (Fig. S65 and S66). In conclusion, with the aid of well-designed monoamine solvation sheath rearrangement additives, the full cells deliver unprecedented electrochemical performance, which proves the significantly facilitated kinetics and repressed side reactions. Besides, the unparalleled capacity and power density realized in the pouch cells promise the practical future of MMBs.

Conclusions

In this work, we discovered that the essence of Mg^{2+} solvation tuning lies in the redistribution of reductive electrons. The high reorganization energy barrier and solvent decomposition for $Mg(TFSI)_2$-based electrolytes are fundamentally caused by the accumulation of reductive electrons on ether molecules, which ultimately hampers the kinetics and electrochemical

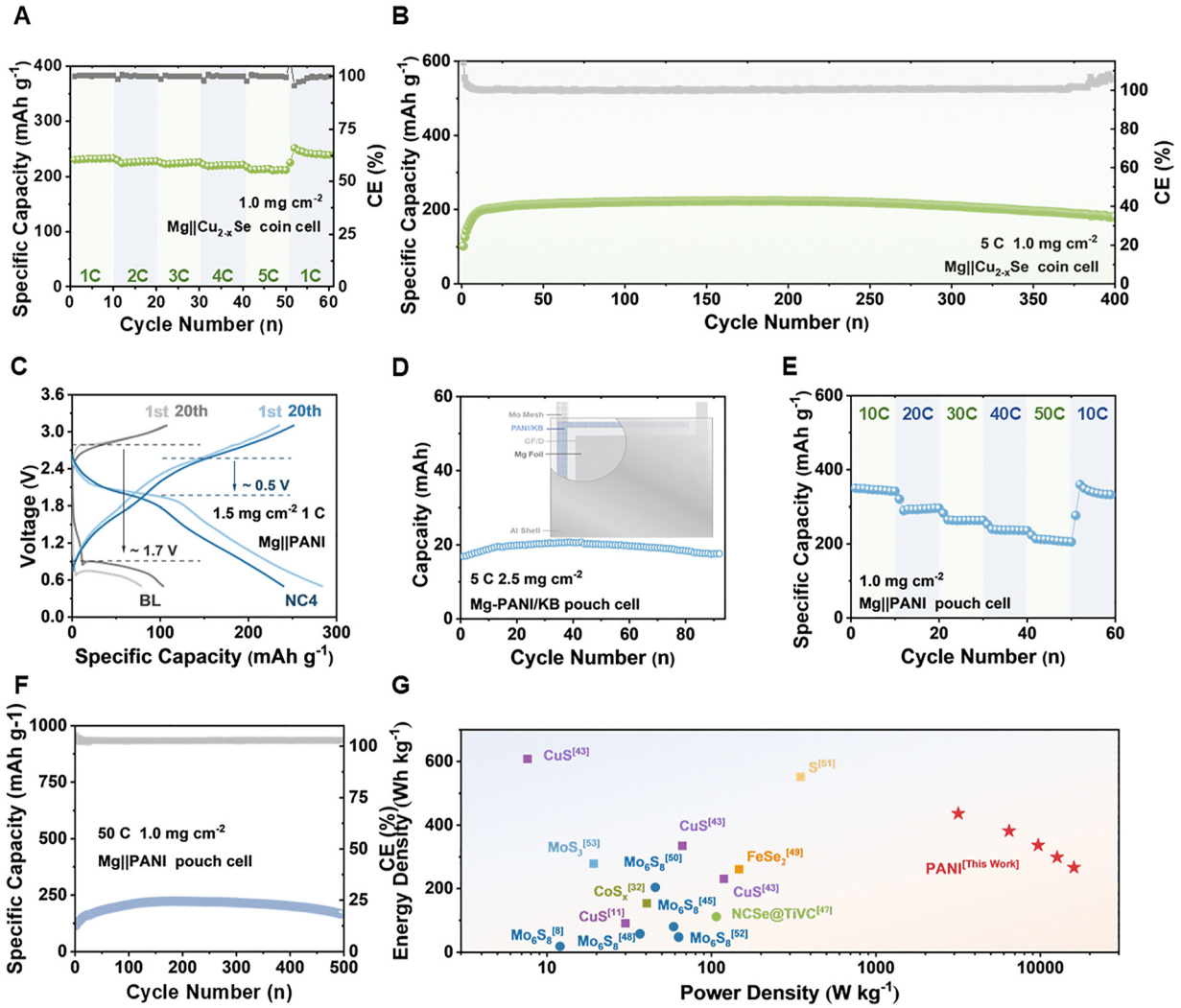

Fig. 4 Electrochemical performance of full cells. (A) Rate performance tests of the $Cu_{2-x}Se$ cathode in the NC4 electrolyte. (B) Cycling performance of the $Cu_{2-x}Se$ cathode in long-term cycling in the NC4 electrolyte at 5C. (C) Discharging-charging voltage curves of the Mg||PANI cells with NC4 and the blank electrolyte. (D) Total capacity of the Mg||PANI pouch cells at 1 C (Inset of Fig. 4d: illustration of the Mg||PANI pouch cell). (E) Rate performance of the Mg||PANI pouch cell. (F) Cycling performance of the Mg||PANI pouch cell with the NC4 electrolyte at a current of 50C. (G) The comparison of energy density and power density of the cathode material in Mg pouch cells between this work and previous research. The energy density and power density of other literatures are estimated and calculated according to the details they provide.

performance. To address these problems, a series of monoamine salts were devised as solvation sheath rearrangement additives, which can capture and stabilize the reductive electrons, thereby boosting the kinetics of the electrolyte effectively. Based on our experimental and theoretical results, we propose the screening guidelines of additives for improving the Mg^{2+} solvation sheath rearrangement effects. The modified electrolyte permits high current tolerance (50C, 13 mA cm^{-2}) in high-capacity pouch cells, resulting in an ultrahigh power density of up to 16.02 kW kg^{-1}, which is hundreds of times higher than those of the previous Mg pouch cells. Our work proposes a direction for designing additives in MMBs with high kinetics and favorable reversibility. It also represents a major breakthrough in the development of Mg pouch cells with high power density, paving the way for the practical application of magnesium batteries.

Methods

Materials

Methylamine, dimethylamine, trimethylamine, tetramethylamine, laurylamine, and methoxyamine hydrochlorides were purchased from Aladdin. $Mg(TFSI)_2$-DME solution (0.5 M), which serves as the blank electrolyte in this work, was purchased from DoDochem. Ketjenblack was bought from Lion Co., Ltd. All kinds of metal sheets used in this work were bought from Guantai Metal Materials Co., Ltd, while the ammonia test kit was bought from Lohand Biological. The thickness of Mg foil, stainless steel, and Mo mesh was 100 mm. Mg foils, the thickness of which was 0.05 mm, were purchased from Yingda Co., Ltd and polished with 500# sandpaper inside an argon-filled glovebox prior to use.

Synthesis

PANI (Aladdin, 98%) was ball-milled with Ketjenblack at a mass ratio of 4 : 5 for 4 h at 300 rpm, and the obtained mixture was ground with polytetrafluoroethylene (10% mass ratio) for 30 min. NMP with an appropriate amount was added for the dissolution, and then the slurry was coated onto the surface of the Mo mesh. The area loading of active materials on the cathode ranged from 1.0 to 2.5 mg cm^{-2}. The cathode was dried at 60 °C in a vacuum oven for 12 hours.

Mo_6S_8 nanoplates were fabricated according to previous research. MoS_2 (Aladdin, 99%), Mo (Aladdin, 98%) and Cu powders (Aladdin, 99%) were ball-milled for 5 h at 400 rpm with the mass ratio of 2 : 1 : 1. The mixture was pressed into 15 × 15 mm^2 tablets at the 50-MPa pressure and then sealed into a Swagelok stainless-steel container in a glovebox filled with Ar. The container was heated to 800 °C for 24 h at a rate of 3 °C min^{-1} and then held at this temperature for an additional 24 h. The products were soaked in 9 M HCl with O_2 bubbling for 24 h. After centrifugation and cleaning, the Mo_6S_8 nanoplates were obtained. The cathode was fabricated by coating and drying the slurry of Mo_6S_8, carbon black and polyvinylidene difluoride at a mass ratio of 7 : 2 : 1 onto the SS and Mo discs. The area loading of Mo_6S_8 was about 1.0 mg cm^{-2}.

$Cu_{2-x}Se$ nanoparticles were synthesized using a straightforward liquid-phase technique. Sodium selenite (Na_2SeO_3, 0.2 mol) and anhydrous sodium sulfate (2 mol) were added to a 100-mL aqueous solution containing 1-mmol sodium dodecyl sulfate (97%, Aladdin) to create solution A. Subsequently, 2 mol of anhydrous sodium sulfate was dissolved in 2 ml of 0.6 M copper(II) acetate monohydrate solution ($Cu(ac)_2{\cdot}H_2O$), and then the mixture was stirred for 10 min to achieve homogeneous solution B. Solutions A and B were mixed and stirred at room temperature for 12 hours, centrifuged, and then washed 3–4 times. The resultant was freeze-dried to obtain powder. The area loading of $Cu_{2-x}Se$ was about 1.0 mg cm^{-2}.

Electrolyte

Methylamine, dimethylamine, trimethylamine, and tetramethylamine hydrochlorides were vacuum-dried at 60 °C, 80 °C, 100 °C, and 130 °C for 24 h, respectively. Then, dried organic monoamine salts were dissolved in 0.5 M $Mg(TFSI)_2$-DME with a concentration of 1.0 M. The formed solution was stirred for 2 h at 60 °C to facilitate the dissolution. The electrolytes used in this work are prepared and stored in the glove box filled with argon, in which concentrations of H_2O and O_2 are controlled to be lower than 0.1 ppm.

Theoretical calculations

GROMACS was applied to simulate the different states of the electrolyte with the addition of monoamine salts. We built the same 4.5 × 4.5 × 4.5 Å box for all the groups, and 200 DME molecules, 20 $TFSI^-$ anions, 20 Mg^{2+}, 20 monoamine molecules and 20 Cl^- were added into it. The Lorentz–Berthelot combination rule was used to compute the LJ interactions for atoms in the simulation. The system initially underwent an energy minimization procedure before the 20-ns MD simulation. In order to integrate the equations of motion, the MD simulation was run in an NPT ensemble at 298 K and 1 bar using a velocity-rescale thermostat and a Berendsen barostat for 30 ps at 0.2 fs each step. Amber99SB was the force field used in this simulation. The trajectory maps were generated by VMD.[55] The input files were generated by Sobtop.[56]

All the quantum chemical calculations were carried out using Gaussian 16.[57] The calculations on solvation structures and their optimization analysis were performed on the 6–311++G(d,p) basis set, while structure optimization was based on b3lyp, and the energy was based on M05-2X, with no any symmetry restrictions. The fragment charges of the solvation sheath were calculated using Multiwfn 3.8, while all the electron distribution pictures were plotted using the same software.[58–60]

All the calculation and simulation images were plotted by VMD and rendered by Tachyon. The reorganization energy was calculated using a four-point method. Specifically, the details of the de-solvation energy calculation are described in Fig. S6. E_{22} and E_{11} represent the energy of stable states for each, respectively. Although E_{12} and E_{21} have the same structure with E_{11} and E_{22}, they are differently charged, with the energy difference denoted as λ_I and λ_{II}. The Marcus electron transfer energy barrier $\Delta G_1^{\neq}$ equals to $(\lambda_I + \lambda_{II})/8$. Moreover, due to the strong interaction between Mg^{2+} and monoamines, DME molecules tend to initially decoordinate. The decoordination energy $\Delta G_2^{\neq}$ represents the energy barrier that needs to be overcome during the decoordination of one chelation site.

The AIMD simulation module integrated within the VASP code was utilized, with a time step of 1 fs, under the NVT ensemble controlled by a Nose–Hoover thermostat. The Brillouin zones were sampled with 2 × 2 × 2 Monkhorst–Pack k-point grids. The molecular structure was positioned in a 20 × 20 × 20 Å box to eliminate the influence of periodic boundary conditions. All AIMD simulations were conducted at a constant temperature of 300 K. The planewave basis-set cutoff was fixed at 450 eV, with energy convergence criteria set to 10^{-4} eV.

Characterizations

The compositional characterizations were mainly carried out *via* XPS (Thermo K-alpha). The XRD tests were conducted using Bruker D8 Advance, with Cu Kα radiation (λ = 0.1542 nm). TOF-SIMS tests were performed on TOF-SIMS 5 IONTOF, while Raman microscopy was performed using LabRAM HR Evolution. The morphology observation and element mapping of the materials were completed using Hitachi Regulus 8100 SEM. The negative mode ESI-MS tests were conducted using Orbitrap Exploris 240. NH_4^+ was detected in the solution using ICS-5000+ (Thermo Fisher Scientific). The ammonia concentration test kit was produced by Lohand Biological.

Electrochemical measurements

Unless stated otherwise, all the electrochemical measurements in this work were conducted in CR2032 coin cells. All the overpotential tests were carried out in Mg||Mg symmetry cells and the CE tests in Mg||SS asymmetry cells. The current used in

symmetry and half-cell tests was 0.1 mA cm^{-2}, and the capacity was 0.1 mAh cm^{-2}, unless otherwise noted. All the Mg||Mg symmetry cells measured in the EIS tests were scanned from 100 kHz to 10 mHz, with an amplitude of 10 mV. The LSV tests of the electrolyte were conducted in the Swagelok cell, the scanning rate of which is listed in the figures. The Mg||PANI pouch cells were assembled and sealed in Al-plastic film. The electrolyte volume in symmetric and half cells was required to be about 150 μL to fully saturate the separator. The electrolyte volume used in full cells was about 50 μL/1 mg PANI. The low-temperature environment used in the capacity tests was created by Greenwood SG-22-CC. The current collector used in the pouch cell was Mo mesh (0.5 mm, 200 mesh), while the anode used was a polished 0.5-mm thick Mg foil. Before being used, the Mg plates were polished using a sand paper (500 mesh, 3M) in the glove box. The size of the Mg anode and PANI/Mo cathode was around 3 × 6 cm^2. The detailed weights of all the components are listed in Table S8. All the components of the pouch cells used in the cell assembly were pre-dried in an oven at 80 °C for 24 h to remove the moisture. They were all assembled in an argon-filled glove box, with the O_2 and H_2O concentrations being always lower than 0.1 ppm. All the electrochemical measurements were carried out at room temperature.

All the discharging/charging performance tests were carried out in a Neware CT-4000 or LAND battery testing system, while all the electrochemical characterizations were conducted using CHI600A. The temperature in the electrochemical tests was maintained at 27 °C. Unless stated otherwise, the current and capacity of Mg||Mg symmetry cells and Mg||SS half cells were 0.1 mA cm^{-2} and 0.1 mAh cm^{-2}, respectively. The frequency in the impedance tests was from 10 kHz to 10 Hz. The scanning rate in the CV and LSV tests was set to 0.1 mV s^{-1}. For LSV tests, the Mg||SS half cells are scanned from the open circuit potential to 3.5 V. For $Cu_{2-x}Se$, Mo_6S_8 and PANI cathode, 1 C refers to 250, 126 and 260 mA g^{-1}, respectively.

Author contributions

Conceptualization, Xuebin Yu and Hongyu Zhang; methodology, Xuebin Yu, Wenbin Wang, Chaoqun Li, and Guanglin Xia; investigation, Wenbin Wang, Xuebin Yu, Miao Guo, Xian Zhou, and Chaoqun Li; writing – original draft, Xuebin Yu, Wenbin Wang, Hongyu Zhang, and Xian Zhou; writing – review & editing, Xuebin Yu, Hongyu Zhang, and Wenbin Wang; funding acquisition, Xuebin Yu; resources, Xuebin Yu; Supervision, Xuebin Yu.

Conflicts of interest

There are no conflicts to declare.

Data availability

The data supporting this article have been included as part of the supplementary information (SI). Supplementary information: Fig. S1–S66, Tables S1–S11, more detailed electrochemical test parameters and further experimental details. They are available at https://doi.org/10.1039/d5ee06320e.

Acknowledgements

This work is funded by the National Sciences Foundation of China (51971065 and 52301265), Innovation Program of the Shanghai Municipal Education Commission (2019-01 07-00-07-E00028) and China Postdoctoral Science Foundation (2023M730616).

References

1 C. K. Chan, H. Peng, G. Liu, K. McIlwrath, X. F. Zhang and R. A. Huggins, *et al.*, High-performance lithium battery anodes using silicon nanowires, *Nat. Nanotechnol.*, 2007, **3**(1), 31–35.
2 P. G. Bruce, S. A. Freunberger, L. J. Hardwick and J.-M. Tarascon, Li–O2 and Li–S batteries with high energy storage, *Nat. Mater.*, 2011, **11**(1), 19–29.
3 V. Etacheri, R. Marom, R. Elazari, G. Salitra and D. Aurbach, Challenges in the development of advanced Li-ion batteries: a review, *Energy Environ. Sci.*, 2011, **4**, 9.
4 Y. Liang, H. Dong, D. Aurbach and Y. Yao, Current status and future directions of multivalent metal-ion batteries, *Nat. Energy*, 2020, **5**(9), 646–656.
5 P. Saha, M. K. Datta, O. I. Velikokhatnyi, A. Manivannan, D. Alman and P. N. Kumta, Rechargeable magnesium battery: Current status and key challenges for the future, *Prog. Mater. Sci.*, 2014, **66**, 1–86.
6 P. Canepa, S. Jayaraman, L. Cheng, N. N. Rajput, W. D. Richards and G. S. Gautam, *et al.*, Elucidating the structure of the magnesium aluminum chloride complex electrolyte for magnesium-ion batteries, *Energy Environ. Sci.*, 2015, **8**(12), 3718–3730.
7 O. Tutusaus and R. Mohtadi, Paving the way towards highly stable and practical electrolytes for rechargeable magnesium batteries, *ChemElectroChem*, 2015, **2**(1), 51–57.
8 A. W. Tomich, J. Chen, V. Carta, J. Guo and V. Lavallo, Electrolyte Engineering with Carboranes for Next-Generation Mg Batteries, *ACS Cent. Sci.*, 2024, **10**(2), 264–271.
9 Z. Zhang, Z. Cui, L. Qiao, J. Guan, H. Xu and X. Wang, *et al.*, Novel design concepts of efficient Mg-Ion electrolytes toward high-performance magnesium–selenium and magnesium–sulfur batteries, *Adv. Energy Mater.*, 2017, **7**(11), 1602055.
10 T. Pavčnik, M. Lozinšek, K. Pirnat, A. Vizintin, T. Mandai and D. Aurbach, *et al.*, On the practical applications of the magnesium fluorinated alkoxyaluminate electrolyte in Mg battery cells, *ACS Appl. Mater. Interfaces*, 2022, **14**(23), 26766–26774.
11 S. Li, J. Zhang, S. Zhang, Q. Liu, H. Cheng and L. Fan, *et al.*, Cation replacement method enables high-performance electrolytes for multivalent metal batteries, *Nat. Energy*, 2024, **9**(3), 285–297.

12 D. Aurbach, Z. Lu, A. Schechter, Y. Gofer, H. Gizbar and R. Turgeman, *et al.*, Prototype systems for rechargeable magnesium batteries, *Nature*, 2000, **407**(6805), 724–727.
13 H. S. Kim, T. S. Arthur, G. D. Allred, J. Zajicek, J. G. Newman and A. E. Rodnyansky, *et al.*, Structure and compatibility of a magnesium electrolyte with a sulphur cathode, *Nat. Commun.*, 2011, **2**(1), 427.
14 T. J. Carter, R. Mohtadi, T. S. Arthur, F. Mizuno, R. Zhang and S. Shirai, *et al.*, Boron clusters as highly stable magnesium-battery electrolytes, *Angew. Chem.*, 2014, **126**(12), 3237–3241.
15 S. Hebié, F. Alloin, C. Iojoiu, R. Berthelot and J.-C. Leprêtre, Magnesium anthracene system-based electrolyte as a promoter of high electrochemical performance rechargeable magnesium batteries, *ACS Appl. Mater. Interfaces*, 2018, **10**(6), 5527–5533.
16 H. Wang, X. Feng, Y. Chen, Y.-S. Liu, K. S. Han and M. Zhou, *et al.*, Reversible electrochemical interface of Mg metal and conventional electrolyte enabled by intermediate adsorption, *ACS Energy Lett.*, 2019, **5**(1), 200–206.
17 W. Zhao, Z. Pan, Y. Zhang, Y. Liu, H. Dou and Y. Shi, *et al.*, Tailoring Coordination in Conventional Ether-Based Electrolytes for Reversible Magnesium-Metal Anodes, *Angew. Chem., Int. Ed.*, 2022, **61**(30), e202205187.
18 A.-M. Li, Z. Wang, T. Lee, N. Zhang, T. Li and W. Zhang, *et al.*, Asymmetric electrolyte design for high-energy lithium-ion batteries with micro-sized alloying anodes, *Nat. Energy*, 2024, 1–10.
19 H. Cheng, Q. Sun, L. Li, Y. Zou, Y. Wang and T. Cai, *et al.*, Emerging era of electrolyte solvation structure and interfacial model in batteries, *ACS Energy Lett.*, 2022, **7**(1), 490–513.
20 P. Xiao, X. Yun, Y. Chen, X. Guo, P. Gao and G. Zhou, *et al.*, Insights into the solvation chemistry in liquid electrolytes for lithium-based rechargeable batteries, *Chem. Soc. Rev.*, 2023, **52**(15), 5255–5316.
21 F. Wang, H. Hua, D. Wu, J. Li, Y. Xu and X. Nie, *et al.*, Solvent molecule design enables excellent charge transfer kinetics for a magnesium metal anode, *ACS Energy Lett.*, 2022, **8**(1), 780–789.
22 Y. Liu, W. Zhao, Z. Pan, Z. Fan, M. Zhang and X. Zhao, *et al.*, Interfacial engineering of magnesiophilic coordination layer stabilizes Mg metal anode, *Angew. Chem.*, 2023, **135**(25), e202302617.
23 M. Wang, W. Sun, K. Zhang, Z. Zhang, A. Du and S. Dong, *et al.*, Synergy between the coordination and trace ionization of co-solvents enables reversible magnesium electroplating/stripping behavior, *Energy Environ. Sci.*, 2024, **17**(2), 630–641.
24 S. Hou, X. Ji, K. Gaskell, P.-F. Wang, L. Wang and J. Xu, *et al.*, Solvation sheath reorganization enables divalent metal batteries with fast interfacial charge transfer kinetics, *Science*, 2021, **374**(6564), 172–178.
25 Z. Li, X. Mu, Z. Zhao-Karger, T. Diemant, R. J. Behm and C. Kübel, *et al.*, Fast kinetics of multivalent intercalation chemistry enabled by solvated magnesium-ions into self-established metallic layered materials, *Nat. Commun.*, 2018, **9**(1), 5115.
26 M. Salama, I. Shterenberg, L. JW Shimon, K. Keinan-Adamsky, M. Afri, Y. Gofer and D. Aurbach, Structural Analysis of Magnesium Chloride Complexes in Dimethoxyethane Solutions in the Context of Mg Batteries Research, *J. Phys. Chem. C*, 2017, **121**(45), 24909–24918.
27 Z. Li, X. Mu, Z. Zhao-Karger, T. Diemant, R. J. Behm and C. Kübel, *et al.*, Fast kinetics of multivalent intercalation chemistry enabled by solvated magnesium-ions into self-established metallic layered materials, *Nat. Commun.*, 2018, **9**(1), 5115.
28 M. Jäckle, K. Helmbrecht, M. Smits, D. Stottmeister and A. Groß, Self-diffusion barriers: possible descriptors for dendrite growth in batteries?, *Energy Environ. Sci.*, 2018, **11**(12), 3400–3407.
29 S.-Y. Ha, Y.-W. Lee, S. W. Woo, B. Koo, J.-S. Kim and J. Cho, *et al.*, Magnesium(II) Bis(trifluoromethane sulfonyl) Imide-Based Electrolytes with Wide Electrochemical Windows for Rechargeable Magnesium Batteries, *ACS Appl. Mater. Interfaces*, 2014, **6**(6), 4063–4073.
30 W. Wang, S. Ju, H. Zhang, X. Zhou and X. Yu, Synchronous regulation on solvation structure and interface engineering to enable reversible magnesium metal batteries, *Energy Storage Mater.*, 2024, **70**, 103493.
31 J. B. Moss, L. Zhang, K. V. Nielson, Y. Bi, C. Wu and S. Scheiner, *et al.*, Computational Insights into Mg-Cl Complex Electrolytes for Rechargeable Magnesium Batteries, *Batteries Supercaps*, 2019, **2**(9), 792–800.
32 A. Maddegalla, Y. Kumar, S. Chakrabarty, Y. Glagovsky, B. Schmerling and N. Fridman, *et al.*, First isolation of solvated MgCl+ species as the sole cations in electrolyte solutions for rechargeable Mg batteries, *Electrochim. Acta*, 2023, **463**, 142869.
33 S. F. Nelsen, S. C. Blackstock and Y. Kim, Estimation of inner shell Marcus terms for amino nitrogen compounds by molecular orbital calculations, *J. Am. Chem. Soc.*, 1987, **109**(3), 677–682.
34 R. A. Marcus, Electron transfer reactions in chemistry: theory and experiment (Nobel lecture), *Angew. Chem., Int. Ed. Engl.*, 1993, **32**(8), 1111–1121.
35 N. Sa, B. Pan, A. Saha-Shah, A. A. Hubaud, J. T. Vaughey and L. A. Baker, *et al.*, Role of chloride for a simple, non-Grignard Mg electrolyte in ether-based solvents, *ACS Appl. Mater. Interfaces*, 2016, **8**(25), 16002–16008.
36 H. Fan, X. Zhang, J. Xiao, Y. Lin, S. Ren and Y. Zhao, *et al.*, Simultaneous optimization of solvation structure and water-resistant capability of MgCl2-based electrolyte using an additive combination of organic and inorganic lithium salts, *Energy Storage Mater.*, 2022, **51**, 873–881.
37 Z. Liang and C. Ban, Strategies to enable reversible magnesium electrochemistry: from electrolytes to artificial solid–electrolyte interphases, *Angew. Chem., Int. Ed.*, 2021, **60**(20), 11036–11047.
38 K. Förster-Tonigold, F. Buchner, J. Bansmann, R. J. Behm and A. Groß, A Combined XPS and Computational Study of

the Chemical Reduction of BMP-TFSI by Lithium, *Batteries Supercaps*, 2022, **5**(12), e202200307.
39 M. G. Olayo, E. J. Alvarado, M. González-Torres, L. M. Gómez and G. J. Cruz, Quantifying amines in polymers by XPS, *Polym. Bull.*, 2024, **81**(3), 2319–2328.
40 Y. Y. Hwang, N. K. Lee, S. H. Park, J. Shin and Y. J. Lee, TFSI anion grafted polymer as an ion-conducting protective layer on magnesium metal for rechargeable magnesium batteries, *Energy Storage Mater.*, 2022, **51**, 108–121.
41 V. Prabhakaran, G. Agarwal, J. D. Howard, S. Wi, V. Shutthanandan and D.-T. Nguyen, *et al.*, Coordination-dependent chemical reactivity of TFSI anions at a Mg metal interface, *ACS Appl. Mater. Interfaces*, 2023, **15**(5), 7518–7528.
42 W. Zhao, Z. Pan, Y. Zhang, Y. Liu, H. Dou and Y. Shi, *et al.*, Tailoring Coordination in Conventional Ether-Based Electrolytes for Reversible Magnesium-Metal Anodes, *Angew. Chem., Int. Ed.*, 2022, **61**(30), e202205187.
43 M. Mao, T. Gao, S. Hou, F. Wang, J. Chen and Z. Wei, *et al.*, High-energy-density rechargeable Mg battery enabled by a displacement reaction, *Nano Lett.*, 2019, **19**(9), 6665–6672.
44 J. A. Blázquez, R. R. Maça, O. Leonet, E. Azaceta, A. Mukherjee and Z. Zhao-Karger, *et al.*, A practical perspective on the potential of rechargeable Mg batteries, *Energy Environ. Sci.*, 2023, **16**(5), 1964–1981.
45 J. Bi, Y. Liu, Z. Du, K. Wang, W. Guan and H. Wu, *et al.*, Bottom-Up Magnesium Deposition Induced by Paper-Based Triple-Gradient Scaffolds toward Flexible Magnesium Metal Batteries, *Adv. Mater.*, 2024, **36**(9), 2309339.
46 J. Wang, T. Ghosh, Z. Ju, M.-F. Ng, G. Wu and G. Yang, *et al.*, Heterojunction structure of cobalt sulfide cathodes for high-performance magnesium-ion batteries, *Matter*, 2024, **7**(5), 1833–1847.
47 Y. Zhang, J. M. Cao, Z. Yuan, H. Xu, D. Li and Y. Li, *et al.*, $TiVCT_x$ MXene/Chalcogenide Heterostructure-Based High-Performance Magnesium-Ion Battery as Flexible Integrated Units, *Small*, 2022, **18**(30), 2202313.
48 X. Ge, F. Song, A. Du, Y. Zhang, B. Xie and L. Huang, *et al.*, Robust Self-Standing Single-Ion Polymer Electrolytes Enabling High-Safety Magnesium Batteries at Elevated Temperature, *Adv. Energy Mater.*, 2022, **12**(31), 2201464.
49 T. Zhou, T. Han, X. Lin, J. Liu, X. Zeng and P. Zhan, *et al.*, Designing a Magnesium/Sodium Hybrid Battery Using Hierarchical Iron Selenide Architecture as Cathode Material and Modified Dual-Ion Salts in Ether as Electrolyte, *Nano Lett.*, 2024, **24**(15), 4400–4407.
50 S. Chen, M. Zhou, D. Zhang, S. Zhang, Y. Zhao and M. Pan, *et al.*, Gel Polymer Electrolytes Based on Facile In Situ Ring-Opening Polymerization Enabling High-Performance Rechargeable Magnesium Batteries, *Adv. Funct. Mater.*, 2024, **34**(48), 2408535.
51 J. Bi, Z. Zhou, J. Li, B. Li, X. Sun and Y. Liu, *et al.*, Enhancing Reversibility and Stability of Mg Metal Anodes: High-Exposure (002) Facets and Nanosheet Arrays for Superior Mg Plating/Stripping, *Angew. Chem., Int. Ed.*, 2024, **63**(37), e202407770.
52 D. Zhang, Y. Sun, X. Liu, Y. Zhang, R. Wang and Y. Zhao, *et al.*, Borohydride-Based Interphase Enabling Reversible Magnesium Metal Anode in Conventional Electrolytes, *ACS Energy Lett.*, 2024, **9**, 2685–2695.
53 Y. Liu, A. Xu, J. Wang, F. Jiang, H. Pang and J. Yang, *et al.*, Amorphous MoS3 Anchored within Hollow Carbon as a Cathode Material for Magnesium-Ion Batteries, *ACS Nano*, 2024, **18**(48), 33197–33209.
54 T. Wen, S. Tan, R. Li, X. Huang, H. Xiao and X. Teng, *et al.*, Large-Scale Integration of the Ion-Reinforced Phytic Acid Layer Stabilizing Magnesium Metal Anode, *ACS Nano*, 2024, **18**(18), 11740–11752.
55 W. Humphrey, A. Dalke and K. Schulten, VMD: visual molecular dynamics, *J. Mol. Graphics*, 1996, **14**(1), 33–38.
56 T. Lu, Sobtop. May, Version 1.0 (dev2), 2022 (Available from: Available online: https://sober eva.com/soft/Sobtop. accessed on 1 2022).
57 M. J. Frisch, G. W. Trucks, H. B. Schlegel, G. E. Scuseria, M. A. Robb and J. R. Cheeseman, *et al. Gaussian 16 Rev. C.01*, Wallingford, CT, 2016.
58 T. Lu and F. Chen, Multiwfn: A multifunctional wavefunction analyzer, *J. Comput. Chem.*, 2012, **33**(5), 580–592.
59 T. Lu, A comprehensive electron wavefunction analysis toolbox for chemists, Multiwfn, *J. Chem. Phys.*, 2024, **161**(8), 082503.
60 J. Zhang and T. Lu, Efficient evaluation of electrostatic potential with computerized optimized code, *Phys. Chem. Chem. Phys.*, 2021, **23**(36), 20323–20328.

